PCCP

Accepted Manuscript

ROYAL SOCIETY OF CHEMISTRY

www.rsc.org/pccp

Journal Name

ARTICLE

Role of S and Se atoms on the microstructural properties of kesterite $Cu_2ZnSn(S_xSe_{1-x})_4$ thin film solar cells

Received 00th January 20xx,
Accepted 00th January 20xx

DOI: 10.1039/x0xx00000x

www.rsc.org/

Mirjana Dimitrievska[a]*, Andrew Fairbrother[a], Rene Gunder[b], Galina Gurieva[b], Haibing Xie[a], Edgardo Saucedo[a], Alejandro Pérez-Rodríguez[a, c], Victor Izquierdo-Roca[a] and Susan Schorr[b, d]

Microstructural properties of $Cu_2ZnSn(S_xSe_{1-x})_4$ kesterite solid solutions were investigated using grazing incidence X-ray diffraction for the full interval of anion compositions in order to explore the influence of S and Se atoms on the thin film morphology. Thin films were prepared by sputtering deposition of metallic precursors, which were then submitted to a high temperature sulfo-selenization process. By adjusting process parameters samples from sulfur- to selenium-pure ($0 \le x \le 1$) were made. Microstructural analysis shows a strong dependence of domain size and microstrain on composition. Both values increase with higher sulfur content, and depth profile analysis by grazing incidence X-ray diffraction shows selenium-rich films tend to have a more homogeneous depth distribution of domain size. The increasing trend in domain size of S-rich absorbers can be related to lower formation energies of the sulfur binary phases leading to formation of kesterites, while the increase in the microstrain is explained by the substitution of larger Se atoms with smaller S atoms in the host lattice and the presence of secondary phases.

Introduction

In order to further grow the role of photovoltaics (PV) in the global energy mix, a number of new materials are being investigated to address the issues of scaling and efficiency, in particular among the second and third generation PV technologies. Within the second generation of light absorbers, kesterites, including Cu_2ZnSnS_4 (CZTS), $Cu_2ZnSnSe_4$ (CZTSe), and their solid solutions $Cu_2ZnSn(S,Se)_4$ (CZTSSe), have garnered interest because of their similarities to chalcopyrites ($Cu(In,Ga)Se_2$), the current thin film efficiency champion.[1] While record device efficiencies of kesterites are still not sufficient for commercialization, the benefits of using compounds composed of earth abundant elements are expected to become significant as photovoltaic energy production increases to much higher levels in the long term. In order to demonstrate kesterite-based solar cells as a viable technology several questions remain to be answered, both from fundamental and applied perspectives.[2]

The highest efficiency kesterite-based devices employ solid solutions (CZTSSe), which contain both sulfur and selenium anions. The current record performance of 12.6% compares well against the significantly lower efficiencies of 9.2% and 11.6% for CZTS and CZTSe respectively,[3–5] thus making them more interesting technologically. The higher efficiency is caused by effective tuning of the bandgap between 1.0 and 1.5 eV due to the changes in the anion composition. Bandgap engineering is crucial for maximizing light absorption and ensuring optimal band alignment with the n-type buffer layer.[6,7] This wide range opens many possibilities for material design, which can help in optimization of the photovoltaic device structure. Several groups have reported synthesis routes for CZTSSe, including solid-state reaction, physical vapor deposition, nanocrystal synthesis, and other solution-based methods including hydrazine.[3,8–13]

First principle calculations on the band structure and optical properties of CZTSSe have indicated that the mixed-anion solutions are highly miscible.[14] The influence of anion composition on structural and optical properties has been experimentally investigated, and a linear change of the lattice parameters and optical bandgap in agreement with Vegard's law has been observed.[15] For thin films a microstructural analysis is necessary to determine properties such as domain size and microstrain, which in turn can influence device performance. Typically a larger domain size is expected to reduce recombination of photogenerated charge carriers due to the lower density of defects, including grain boundaries.[16–19] However, this has not always been shown to be true, and in fact the grain boundaries may actually play a beneficial role by passivating other defects.[20] Strain can also influence performance of a device, and the mechanical properties of kesterites are poorly understood. Such knowledge is valuable due to the multi-layer nature of a solar cell device, in which mechanical failure such as delamination would effectively

[a] Catalonia Institute for Energy Research (IREC), Jardins de les Dones de Negre 1, 08930 Sant Adrià de Besòs, Spain.
[b] Helmholtz Centre Berlin for Materials and Energy, Department Crystallography, Hahn-Meitner-Platz 1, 14109 Berlin, Germany.
[c] IN²UB, University of Barcelona, C. Martí Franquès 1, 08028 Barcelona, Spain
[d] Freie Universität Berlin, Institute of Geological Sciences, Malteserstr. 74-100, 12249 Berlin, Germany.
*Contact email: mdimitrievska@irec.cat, mira.dimitrievska@gmail.com

destroy the device. The most basic thin film solar cells consist of at least six layers – substrate, back contact, absorber, buffer, and front contact – and the interface between each layer plays a significant role in overall performance, as excessive strain not only leads to delamination, but can also alter optical and electronic properties.

In this work the microstructure of CZTSSe thin films covering the full range of anion compositions was studied by X-ray diffraction (XRD). Thin films were prepared by DC-magnetron sputtering deposition of metallic precursors, which were then submitted to a high temperature sulfo-selenization process. By adjusting process parameters samples from sulfur- to selenium-pure ($0 \le [S] / ([S] + [Se]) \le 1$) were prepared. Microstructural analysis showed a strong dependence of the domain size and microstrain on anion composition. Both values increase with higher sulfur content, and depth profile analysis by grazing incidence XRD (GIXRD) shows significant differences in the depth distribution of microstructural properties from selenium rich and sulfur rich films.

Experimental

Thin film formation

Kesterite thin films have been prepared by sulfo-selenization of precursor Cu/Sn/Cu/Zn metallic stacks sputter deposited onto Mo-coated soda-lime glass (Ac450 Alliance Concepts). The cation composition was approximately constant for all films, with [Cu] / ([Zn] + [Sn]) = 0.75-0.80 and [Zn] / [Sn] = 1.16-1.22. This range was chosen because it corresponds to that of the highest efficiency kesterite-based solar cells, specifically, Cu-poor and Zn-rich conditions. Precursors were annealed with varying ratios of sulfur and selenium to form CZTSSe with different anion compositions, including pure CZTS and CZTSe. For this step samples were placed in a graphite box with an interior volume of 23.5 cm^3, along with 5 mg of tin power (Alfa Aesar, 99.999%) and 50 mg of chalcogen (sulfur – Alfa Aesar 99.995%, selenium – Alfa Aesar 99.999%), and placed in a tube furnace with a controlled atmosphere. The addition of elemental tin to the process is to suppress Sn-loss from the films during annealing. CZTS was synthesized utilizing only sulfur and tin, and annealed at 550 ^oC for 30 min with a constant background pressure of 1 bar Ar. CZTSe was formed by annealing with selenium and tin at 550 ^oC for 30 min under flowing Ar with a background pressure of 1 mbar. Finally, CZTSSe films were formed in a sulfo-selenization process using a mixture of sulfur and selenium, and annealed at 550 ^oC for 30 min with an Ar background pressure of 1 mbar (flowing) or 1 bar (fixed). In all cases the ramp rate was 20 ^oC/min, and cooled naturally to about 350 ^oC before opening the furnace. By adjusting the ratio of sulfur to selenium in the annealing atmosphere, as well as the total system pressure, it was possible to synthesize films in the full range of anion compositions, including sulfur- and selenium-pure. Further details of the processes employed are published elsewhere.[11]

All films are approximately 1.5 μm thick after the chalcogenation annealing step.

As-grown sulfur-rich films were submitted to an HCl etch,[21] and selenium-rich films to an etch in $KMnO_4/H_2SO_4$+Na_2S,[22] in order to remove surface Zn(S,Se) secondary phases which commonly form under the imposed Zn-rich conditions. Solar cells fabricated using this process have yielded efficiencies of up to 8.6%.

Characterization

The composition of precursor and annealed films was measured by X-ray fluorescence spectroscopy (XRF) (Fischerscope XVD).

Microstructural analysis was performed by grazing incidence X-ray diffraction (GIXRD) measured on a PANalytical X'pert Pro MPD diffractometer with Cu−Kα -radiation (λ=1.54056 Å). Depth profile information was obtained by performing detector scans with fixed incidence angle of 0.5, 1, 2 and 5^o. In the GIXRD configuration, X-ray penetration depth is controlled by the incident angle and can be calculated based on the incident angle and material parameters. Conventionally, penetration depth is defined as the depth where the intensity of X-rays is reduced to 1/e (about 37%) of the original intensity at the surface. Based on the schematic diagram showing X-ray penetration in a sample in GIXRD geometry (Figure S1 in Supporting Information) and the attenuation law, the penetration depth of X-rays, *z*, in kesterite materials can be calculated according to the equation:

$$z = \frac{1}{\mu}\left(\frac{1}{\sin\alpha_i} + \frac{1}{\sin(2\theta - \alpha_i)}\right)^{-1} \quad (1)$$

where α_i is the incidence angle, 2θ is the Bragg angle, and μ is the attenuation coefficient. The attenuation coefficients of CZTSSe compounds were obtained according to simple additivity of the elemental mass attenuation coefficients, $(\mu/\rho)_i$:

$$\mu(\mathrm{CZTSSe}) = \rho(\mathrm{CZTSSe})\sum_i \frac{M_i}{M(\mathrm{CZTSSe})}(\mu/\rho)_i \quad (2)$$

where M_i is the mass fraction of the certain element in the CZTSSe compound, and the M(CZTSSe) is the full mass of the CZTSSe molecule. ρ(CZTSSe) is the density of the CZTSSe samples, calculated as:

$$\rho(\mathrm{CZTSSe}) = x\rho(\mathrm{CZTS}) + (1-x)\rho(\mathrm{CZTSe}) \quad (3)$$

where ρ(CZTS) = 4.57 g/cm^3 and ρ(CZTSe) = 5.69 g/cm^3 are densities of pure CZTS and CZTSe materials,[23] and *x* is the [S] / ([S] + [Se]) ratio. The values for the elemental mass attenuation coefficients, $(\mu/\rho)_i$, of Cu, Zn, Sn, S and Se for the Cu−Kα radiation energy were taken from Ref. [24].

Penetration depths for 0.5, 1, 2 and 5^o incidence angles were calculated according to Eq. (1) for different [S] / ([S] + [Se]) compositions and presented in Figure 1.

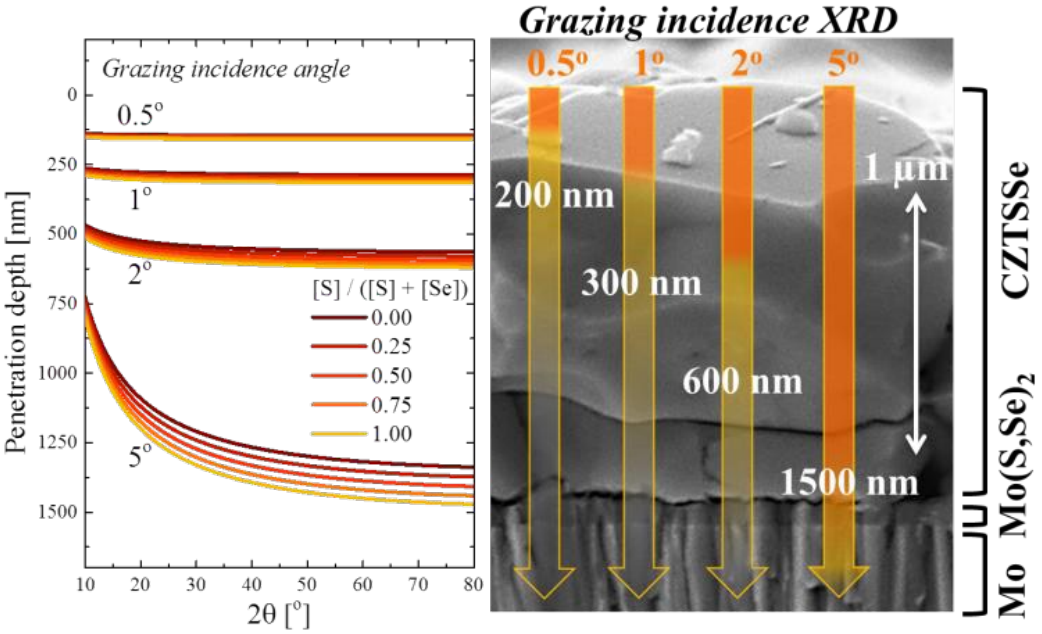

Figure 1. Estimated penetration depths for different grazing incidence angles for CZTS, CZTSe, and CZTSSe, calculated from Eq. (1), and illustration of X-ray penetration in an SEM cross sectional image of CZTSSe.

The collected GIXRD pattern were analysed by a Le Bail refinement using the FullProf Suite software.[25] The Thompson-Cox-Hastings pseudo-Voigt function was applied to describe the GIXRD peak shape profile and to calculate microstructural parameters of domain size and microstrain.[26] Cross sectional SEM was made with 20 kV acceleration voltage on a ZEISS Series Auriga microscope.

Microstructural analysis of X-ray diffraction data

The analysis of diffraction data can be divided into two methods. The first method involves the calculation of reflection intensities from a structural model which is often referred to as the Rietveld method.[27] Although the principles behind the Rietveld refinement method are quite simple, the use of this technique requires some expertise. This is due to the fact that Rietveld refinement uses a least-squares minimization technique, which can be easily stuck in false minima. Additionally, a bad starting point or correlation among the model parameters could cause divergence early in the refinement procedure. This is why, when using this type of refinement, it is important to take special care with the number of parameters to be refined, to fix some of them or to make constraints. On the other side, a simpler method for refining the XRD patterns, which can be used without the prior knowledge of the crystal structure of the material in detail, is referred to as profile matching method (Le Bail method). In this analysis procedure the structure factors $F_{hkl,}$ which are deduced from the given space group, are initially set to arbitrary values. They evolve iteratively according to the estimations obtained by apportioning data values amongst the contributing reflections.[28] The Le Bail method is usually used if the crystal structure is not known in detail or is difficult to describe, like in the case of disordered structures, or when experimental artifacts are difficult to model. Additionally, the Le Bail method could be used before the Rietveld refinement in order to determine accurately the profile shape function, background, and unit cell parameters. The Rietveld refinement can provide more detailed information about the crystal structure of the material than the other method, such as atomic positions, bond lengths, bond angles, temperature factors, isotropic or anisotropic displacement parameters, etc. However, in cases where these parameters do not play an important role, like in comparative microstructural analysis, it is sufficient to employ only the Le Bail refinement.

In order to have a proper microstructure analysis, it is necessary to do an accurate modeling of the shapes of the XRD peaks. The peak shapes are in this case treated using the Thompson-Cox-Hastings (TCH) pseudo-Voigt function with inclusion of the Finger's treatment of the axial divergence.[26,29] The TCH pseudo-Voigt function is defined as a linear combination of a Lorentzian and a Gaussian function, where each of them have different half width at half maximum parameters, H_L and H_G, respectively. These are calculated in dependence on the diffraction angle θ, using the relations:[30]

$$H_G = \left(U\tan^2\theta + V\tan\theta + W + I_G/\cos^2\theta\right)^{1/2}$$
$$H_L = X\tan\theta + \mathrm{Y}/\cos\theta \qquad (4)$$

where *U*, *V*, *W*, *X*, *Y*, I_G and *Z* are refinable parameters. Besides this, the measured intensity profile $h(x)$ is a convolution of the physical intensity profile from the sample, $f(x)$, with the profile representing instrumental contributions, $g(x)$,

$$h(x) = \int g(x') \cdot f(x - x')dx' \ . \quad (5)$$

So the first step in the line-broadening analysis is to separate the instrumental contribution from the measured line widths. The halfwidth parameters of the instrumental profile function $g(x)$, H_{gG} and H_{gL}, are determined by measuring a standard sample with previously known microstructural properties, under the same conditions and applying the same refinement procedure as for the investigated samples. The instrumental broadening was determined by measuring the standard reference material LaB_6 (SRM 660b), which has no effect on the line broadening due to domain size or microstrain. The halfwidth at half maximum values of the peaks of the sample profile function $f(x)$, are obtain by Eq. (6):

$$\begin{aligned} H_{fL} &= H_{hL} - H_{gL} \\ H_{fG}^2 &= H_{hG}^2 - H_{gG}^2 \end{aligned} \quad (6)$$

where H_{fG} and H_{fL} are halfwidth parameters of the sample profile function, $f(x)$, and H_{hG} and H_{hL} are halfwidth parameters of the measured intensity profile $h(x)$. In this work the ratios of the instrumental and measured peak broadening are 0.2-0.3 for the Lorentzian contribution, and slightly higher for the Gaussian contribution. The higher ratio for the Gaussian contribution is expected because instrumental broadening caused by the optical elements is mostly of the Gaussian nature.

The broadening of a Bragg peak in comparison to the instrumental resolution is due to the presence of microstrain, small domain sizes, and/or defects within the grains. In the case of constant wavelength experimental conditions, the parameters Y and I_G define the domain size, while the parameters X and U are related to the microstrain,[31] as presented in the Eq. (7):

$$\begin{aligned} H_{\varepsilon G}^2 &= U \tan^2\theta \\ H_{dG}^2 &= I_G / \cos^2\theta \\ H_{\varepsilon L} &= X \tan\theta \\ H_{dL} &= Y / \cos\theta \end{aligned} \quad (7)$$

where H_{dG}^2 and $H_{\varepsilon G}^2$ present Gauss-size and Gauss-strain broadening component, while H_{dL}^2 and $H_{\varepsilon L}^2$ present Lorentz-size and Lorentz-strain broadening component. In order to include both the Gaussian and the Lorentz broadening effects in the calculations of the microstructural parameters, the overall size-broadening H_d and microstrain-broadening H_ε are calculated by the weighted averaging:

$$\begin{aligned} H_d &= \begin{pmatrix} H_{dG}^5 + AH_{dG}^4 H_{dL} + BH_{dG}^3 H_{dL}^2 + \\ + CH_{dG}^2 H_{dL}^3 + DH_{dG} H_{dL}^4 + H_{dL}^5 \end{pmatrix} \\ H_\varepsilon &= \begin{pmatrix} H_{\varepsilon G}^5 + AH_{\varepsilon G}^4 H_{\varepsilon L} + BH_{\varepsilon G}^3 H_{\varepsilon L}^2 + \\ + CH_{\varepsilon G}^2 H_{\varepsilon L}^3 + DH_{\varepsilon G} H_{\varepsilon L}^4 + H_{\varepsilon L}^5 \end{pmatrix} \end{aligned} \quad (8)$$

where A, B, C and D are coefficients with the values as defined in Ref. [31]. The weighted domain size d is then calculated according to the Scherrer equation:

$$d = k\lambda / \left(H_d(2\theta)\cos\theta\right) \quad (9)$$

where λ is the wavelength and k is the dimensionless shape factor. On the other side, the average microstrain ε is calculated from:

$$\varepsilon = H_\varepsilon(2\theta) / \tan\theta \ . \quad (10)$$

This work applies the above described method for calculating domain size and microstrain of CZTSSe solid solutions in the full range of anion compositions.

Results and discussion

First, representative GIXRD patterns of the CZTSSe solid solutions (2° GI angle), presented in Figure 2(a), are discussed. The systematic shift in peak position toward lower angles as the [S] / ([S] + [Se]) ratio increases correlates with the replacement of smaller S atoms with larger Se atoms. Furthermore, the presence of a single 112 diffraction peak in all measured diffractograms implies that all samples are homogeneously alloyed rather than a heterogeneous mixture of CZTS and CZTSe phases.[32]

The anion compositions of the samples were obtained based on the position of the 112 diffraction peak and the use of Vegard's law applied for the pure CZTS and CZTSe compounds. Additionally, the lattice parameters a and c of the mixed compounds were calculated based on the Le Bail analysis. In this case, the kesterite structure (space group $I\bar{4}$) was used as the starting model for the refinement procedure, since it has been shown that both CZTS and CZTSe adopt the kesterite type structure.[13,33] Figure S2 in the Supporting Information presents Le Bail fits of the XRD patterns measured with 0.5, 1, 2 and 5° incidence angles of two representative CZTSSe samples with S-rich and Se-rich compositions. For all samples the obtained χ^2 values are below 1.7, indicating good fits of the patterns. The dependence of lattice parameters on the [S] / ([S] + [Se]) ratio is presented in Figure 2(b). The decrease in lattice parameters with increasing S content is caused by shrinkage of the unit cell due to the substitution of Se atoms with S, which have a smaller ionic radius compared to that of Se.

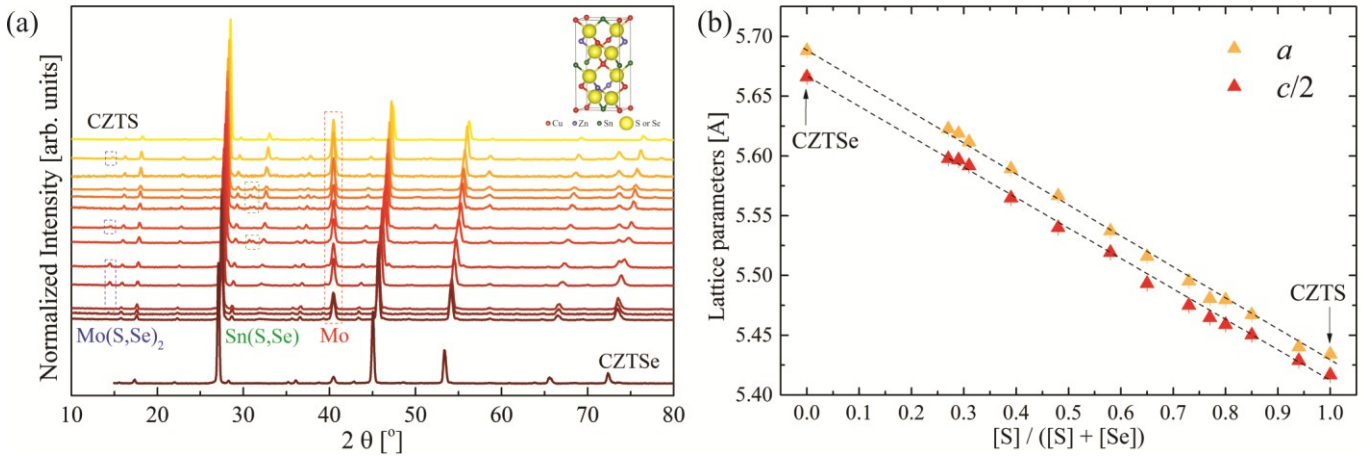

Figure 2. (a) GIXRD patterns of CZTSSe solid solutions measured with 2° GI angle (b) Lattice parameters in dependence of anion [S] / ([S] + [Se]) composition ratio.

In order to perform a reliable microstructural study on these films, an assessment of the presence of secondary phases in the samples has to be made first. All samples used in this work were prepared with Cu-poor ([Cu] / ([Zn] + [Sn]) < 1) and Zn-rich ([Zn] / [Sn] > 1) compositions, which have been shown both theoretically and experimentally to enhance the performance of the kesterite-based devices.[34,35] These conditions increase the probability of forming Zn(S,Se) and Sn-(S,Se), while suppressing formation of Cu-(S,Se) and Cu-Sn-(S,Se) secondary phases. In previous work complete identification of secondary phases was performed by the correlated application of XRD and multiwavelength excitation Raman spectroscopy.[11,36] Raman spectroscopy is a surface sensitive technique, with penetration depths in CZTSSe of up to 100-150 nm for laser excitations with energy higher than 2.2 eV (UV, blue and green wavelengths).[37] On the other hand, XRD is more suitable for bulk characterization, as already shown in Figure 1. The combination of both methods enables localization of the secondary phases, either on the surface or in the bulk of the CZTSSe absorber.[36]

In addition to the presence of kesterite as a major phase in all thin films, the presence of a Sn(S,Se) secondary phase was observed in the XRD patterns of several samples which had a slightly richer Sn compositions when compared to the others. In order to identify the location of this secondary phase in the absorber, Raman measurements with 532 nm excitation were performed on the surface and back region of the kesterite films. Raman spectra of the surface and back region of two representative CZTSSe samples with S-rich and Se-rich compositions are shown in Figure S3 in Supporting Information. The Sn(S,Se) phase was not detected in either region in the whole series of investigated samples, leading to the conclusion that this phase is mostly located in the bulk of the layers. This is further confirmed by the absence of this phase in the XRD patterns measured with lower GI angles, which correspond to near surface area of the samples (Figure 3(b)). While secondary phases often accumulate on the front or back of these films, it is not uncommon for them to form in the bulk, especially along grain boundaries or voids in the film.[38,39] Additionally, no traces of Cu-(S,Se) phases were observed, either by XRD or Raman measurements. Lastly, Raman measurements under resonant conditions were conducted on the surface and back of the absorbers in order to identify the possible presence of Zn(S,Se) phases,[40] as these phases are not readily detectable by XRD due to their structural similarities with CZTSSe. These measurements have confirmed the absence of Zn(S,Se) phases on the surface of the films, as expected due to the etching performed for these secondary phases. On the other side, in the case of S-rich samples, Zn(S,Se) was detected at the back region of the absorbers, which is to be expected according to the previously reported results.[11,34] In addition, formation of the $Mo(S,Se)_2$ phase was observed at the interface with the back contact in both Raman and XRD measurements. The potential effect of the secondary phases on the microstructural properties will be later taken into consideration when discussing the microstructural results.

The compositional uniformity through the thickness of CZTSSe thin films was investigated by the GIXRD measurements with 0.5, 1, 2, and 5° angles. Figures 3(a) and 3(b) present representative diffractograms measured from S-rich and Se-rich samples. No significant shift in peak positions with the change in grazing incidence angles were observed (inset in Figure 3 presents the peak positions of the 112 reflection with the variation of GI angle). Additionally, lattice parameters obtained from the Le Bail analysis have proven to be constant within the experimental error for all grazing incidence angles (Figure 3(c)). Moreover, assessment of the [S] / ([S] + [Se]) composition of the surface and back region of CZTSSe thin films was made based on the Raman spectra measured on these regions and using methodology presented in Ref. [41]. Raman spectra of the surface and back region of the representative samples with the calculated anion compositions are shown in Figure S3 in Supporting Information. The results have not shown any notable difference in the anion composition of the surface and back of the thin films.

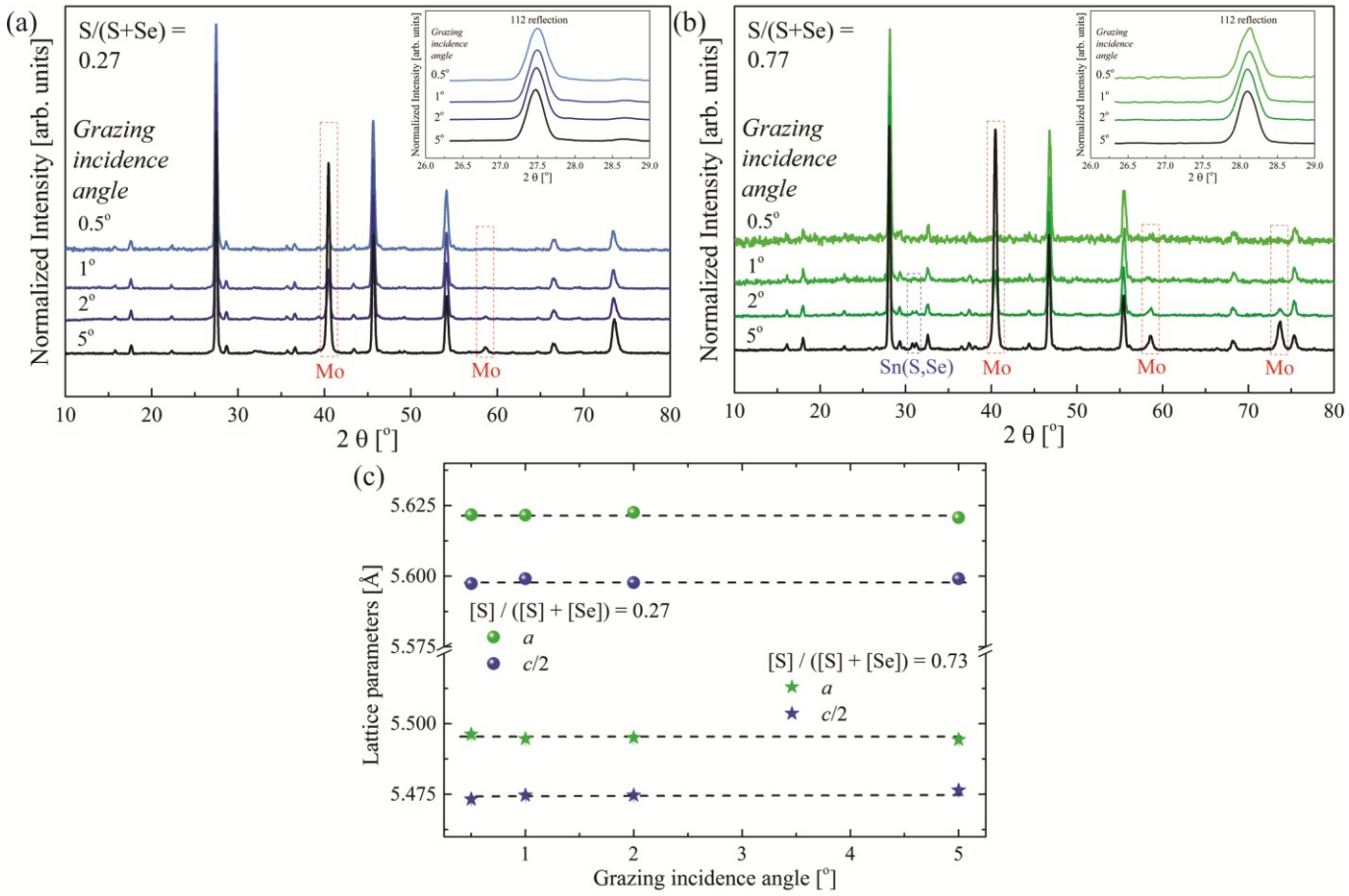

Figure 3. Representative diffraction patterns of CZTSSe solid solutions ((a) [S] / ([S] + [Se]) = 0.27 and (b) [S] / ([S] + [Se]) = 0.77) measured with different GI angles. Inset shows the peak position of the 112 reflection with the change in GI angles. (c) Lattice parameters in dependence of grazing incidence angle are determined by Le Bail refinements. No significant shift in peak position or change in the lattice parameters was detected.

This behavior points out the absence of significant changes in the [S] / ([S] + [Se]) composition through the thickness of the layers. This also points out that the changes in the microstructural properties through the thickness of the absorber are not due to the variation of the anion composition of the CZTSSe layers.

A microstructural analysis based on the Williamson-Hall method[42] and principles presented in the experimental section was performed in order to calculate the average domain size and microstrain of the CZTSSe thin films. The combined analysis shows an increase in domain size and microstrain with increasing [S] / ([S] + [Se]) ratio, as presented in Figure 4(a). The increase in domain size of S-rich absorbers may be related to the lower formation energies of the S-based kesterite precursors, namely binary compounds of Cu, Zn, and Sn.[43] This would mean that these phases form earlier during the short annealing process, and thus grain growth is able to occur over a longer time scale than for Se-rich kesterites and its precursor phases. Additionally, the thermal activation energies for grain growth may also be lower, though very little information on the thermal properties of kesterites is available. Microstrain increases for the S-rich compositions suggests that smaller S atoms are able to substitute larger Se atoms in the structure, resulting in a compressive strain in the crystal structure of CZTSSe. Additionally, a lattice mismatch between the kesterite phase and the substrate, as well as the kesterite and the secondary phases which are present in the bulk of the absorber could lead to increased values of strain for samples in which these phases were detected, such as S-rich samples.

The analysis with different GI angles for each sample gives information about different depth volumes. As illustrated in Figure 1, the lowest GI angle (0.5°) has an estimated penetration depth of 200 nm (1/e of initial X-ray intensity is attenuated), while the highest GI angle (5°) penetrates the entire bulk of the film, 1500 nm. Thus information obtained from the lower angles is indicative mostly of the surface of the films, while at higher angles progressively deeper volumes of the material is analyzed. This analysis shows a decrease in domain size from surface to the back of film for all samples (Figure 4(b)). Larger domain sizes on the surface of the films are expected due to the preparation method, where during the annealing step, S and Se vapors penetrate through the surface of the films, thus promoting the growth of grains at the top. This kind of morphology was also reported for kesterite CZTSSe films prepared by solution-based deposition approaches.[44–46] A similar behavior tends to occur for the

microstrain (Figure 3(c)), and even in this case the sample with lowest [S] / ([S] + [Se]) content has a minimum strain at a grazing incidence angle of 2°. Interestingly, a constant value of microstrain, independent of the anion compositional ratio of the films, is observed for the measurements made with 5° GI angle. This is explained by the constant presence of $Mo(S,Se)_2$ phase, formed at interface with the back contact, which creates a uniform strain, similar in all samples, regardless of the compositional change in the CZTSSe layers.

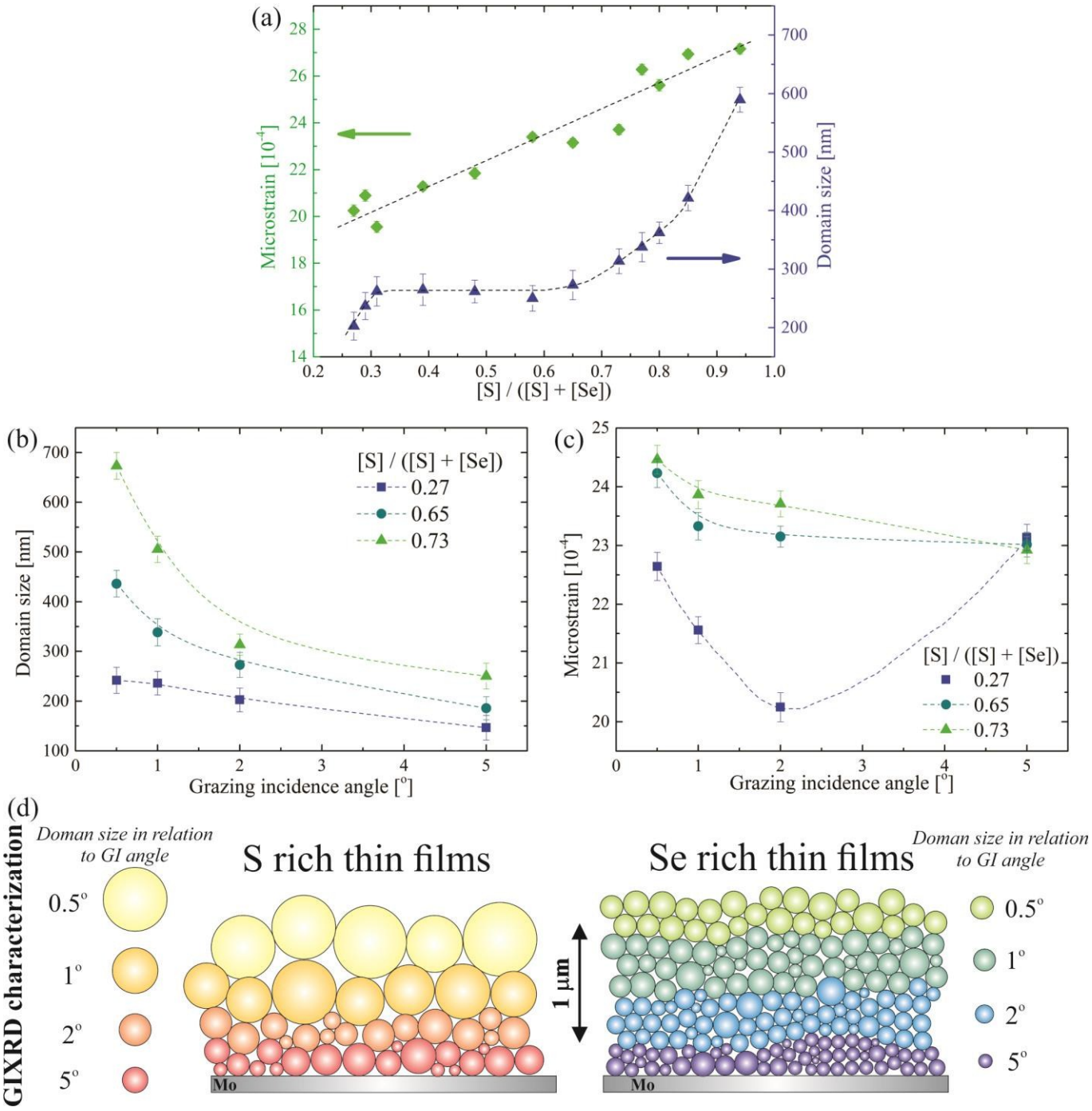

Figure 4. (a) Domain size and microstrain in relation to ([S] / ([S] + [Se]) ratio obtained from the microstructural analysis done for the GIXRD patterns measured with 2° grazing incidence angle. Domain size (b) and micro strain (c) in relation to GI angles for different ([S] / ([S] + [Se]) compositional ratios. Dashed lines are guides for eyes. (d) Proposed model for the domain size distribution of CZTSSe thin films based on GIXRD characterization of S-rich and Se-rich CZTSSe thin films.

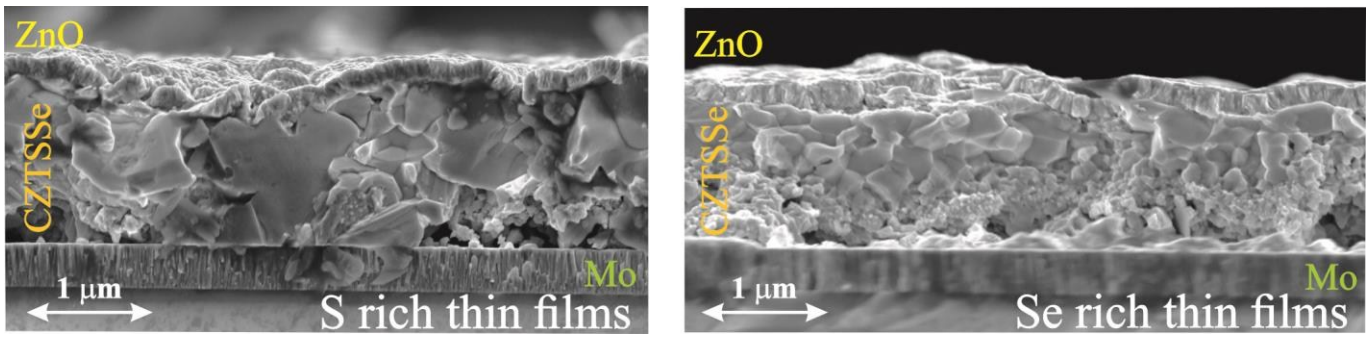

Figure 5. Cross sectional SEM images of S-rich ([S] / ([S] + [Se]) = 0.73) and Se-rich (([S] / ([S] + [Se]) = 0.27) CZTSSe thin films.

Based on the GIXRD characterization, a model for the morphological representation of the cross section for Se-rich and S-rich could be proposed as illustrated in Figure 4(d). It is concluded that Se-rich films are more homogeneous in domain size and show lower microstrain values in comparison to S-rich films.

This behavior is confirmed by SEM images of cross sections for the mentioned films (presented in Figure 5), where a gradual decrease in the grain size from surface to the back of the films is observed for both S- and Se-rich samples. It is also very clear that the larger grains are present in S-rich films when compared to Se-rich films, which is also in agreement with the microstructural study. It should be mentioned that domain size is a measure of the size of coherently scattering domains, which due to the polycrystalline aggregates, is not generally the same as grain size, but it is expected that the observed trends should be similar. Having in mind this, the large difference in the grain size between S-rich and Se-rich films obtained from SEM analysis is in accordance with the large difference in domain size observed from the microstructural analysis of the GIXRD measurements.

Conclusions

A complete analysis of microstructural properties based on GIXRD measurements with various grazing incidence angles was performed for $Cu_2ZnSn(S_xSe_{1-x})_4$ solid solutions. Structural properties show sensitivity to change in the anion composition, by decreasing the lattice parameters with increasing [S] / ([S] + [Se]) ratio. A gradual increase in domain size and microstrain was observed with the transition from Se- to S-rich compounds in the case of samples prepared by sulfo-selenization of sputter deposited metallic precursors. The increasing trend in domain size of S-rich absorbers can be related to the lower formation energies of the CZTS precursors, while the increase in microstrain was explained by the substitution of larger Se atoms with smaller S atoms in the host structure and presence of secondary phases. Additionally, a depth profile structural study showed a gradual decrease in the domain size from the surface to the back of the film, leading to the conclusion that Se-rich CZTSSe films are more homogenous in domain size and with lower values of strain than the S-rich CZTSSe absorbers. As microstructural parameters, through the morphology of the films, play a significant role on device properties in general, these results should provide useful insights for the optimization of the preparation processes of CZTSSe kesterite thin films, which are necessary in order to achieve high efficiency solar cells.

Acknowledgements

The research leading to these results has received funding from the People Program (Marie Curie Actions) of the European Union's Seventh Framework Program FP7/2007-2013/ under REA grant agreement n°316488 (KESTCELLS) and from Spanish MINECO (Ministerio de Economía y Competitividad de España) under the SUNBEAM project (ENE2013-49136-C4-1-R). Authors from IREC and IN2UB belong to the M-2E (Electronic Materials for Energy) Consolidated Research Group and the XaRMAE Network of Excellence on Materials for Energy of the "Generalitat de Catalunya". E.S. thanks the Spanish Ministry of Economy and Competitiveness (MINECO) for the "Ramon y Cajal" Fellowship (RYC-2011-09212. H. X. thanks support from the "China Scholarship Council" fellowship (CSC Nº 201206340113).

References

1 M. A. Green, K. Emery, Y. Hishikawa, W. Warta and E. D. Dunlop, *Prog. Photovolt. Res. Appl.*, 2015, **23**, 1–9.
2 D. S. Ginley and D. Cahen, Eds., *Fundamentals of Materials for Energy and Environmental Sustainability*, Cambridge University Press, Cambridge, 2011.
3 W. Wang, M. T. Winkler, O. Gunawan, T. Gokmen, T. K. Todorov, Y. Zhu and D. B. Mitzi, *Adv. Energy Mater.*, 2014, **4**, 7.
4 Y. S. Lee, T. Gershon, O. Gunawan, T. K. Todorov, T. Gokmen, Y. Virgus and S. Guha, *Adv. Energy Mater.*, 2014, **5**, 7.
5 T. Kato, H. Hiroi, N. Sakai, S. Muraoka and H. Sugimoto, *Proc. 27th Eur. Photovolt. Sol. Energy Conf. Exhib.*, 2012, 2236–2239.
6 S. Chen, A. Walsh, X.-G. Gong and S.-H. Wei, *Adv. Mater.*, 2013, **25**, 1522–1539.
7 S. Chen, X. G. Gong, A. Walsh and S.-H. Wei, *Appl. Phys. Lett.*, 2010, **96**, 021902–021902–3.
8 G. Larramona, S. Levcenko, S. Bourdais, A. Jacob, C. Choné, B. Delatouche, C. Moisan, J. Just, T. Unold and G. Dennler, *Adv. Energy Mater.*, 2015, **5**, 24.
9 S. Singh, P. Liu, A. Singh, C. Coughlan, J. Wang, M. Lusi and K. M. Ryan, *Chem. Mater.*, 2015, **27**, 4742–4748.

10 K. V. Gurav, S. W. Shin, U. M. Patil, M. P. Suryawanshi, S. M. Pawar, M. G. Gang, S. A. Vanalakar, J. H. Yun and J. H. Kim, *J. Alloys Compd.*, 2015, **631**, 178–182.
11 H. Xie, M. Dimitrievska, X. Fontané, Y. Sánchez, S. López-Marino, V. Izquierdo-Roca, V. Bermúdez, A. Pérez-Rodríguez and E. Saucedo, *Sol. Energy Mater. Sol. Cells*, 2015, **140**, 289–298.
12 O. P. Singh, N. Vijayan, K. N. Sood, B. P. Singh and V. N. Singh, *J. Alloys Compd.*, 2015, **648**, 595–600.
13 G. Gurieva, M. Dimitrievska, S. Zander, A. Pérez-Rodríguez, V. Izquierdo-Roca and S. Schorr, *Phys. Status Solidi C*, 2015, **12**, 588–591.
14 A. Khare, B. Himmetoglu, M. Cococcioni and E. S. Aydil, *J. Appl. Phys.*, 2012, **111**, 123704.
15 M. Dimitrievska, H. Xie, A. Fairbrother, X. Fontané, G. Gurieva, E. Saucedo, A. Pérez-Rodríguez, S. Schorr and V. Izquierdo-Roca, *Appl. Phys. Lett.*, 2014, **105**, 031913.
16 H. Guo, Y. Cui, Q. Tian, S. Gao, G. Wang and D. Pan, *Cryst. Growth Des.*, 2015, **15**, 771–777.
17 B. D. Chernomordik, A. E. Béland, D. D. Deng, L. F. Francis and E. S. Aydil, *Chem. Mater.*, 2014, **26**, 3191–3201.
18 M. Johnson, S. V. Baryshev, E. Thimsen, M. Manno, X. Zhang, I. V. Veryovkin, C. Leighton and E. S. Aydil, *Energy Env. Sci*, 2014, **7**, 1931–1938.
19 M. Dimitrievska, A. Fairbrother, A. Pérez-Rodríguez, E. Saucedo and V. Izquierdo-Roca, *Acta Mater.*, 2014, **70**, 272 – 280.
20 H. Xin, S. M. Vorpahl, A. D. Collord, I. L. Braly, A. R. Uhl, B. W. Krueger, D. S. Ginger and H. W. Hillhouse, *Phys Chem Chem Phys*, 2015, **17**, 23859–23866.
21 A. Fairbrother, E. García-Hemme, V. Izquierdo-Roca, X. Fontané, F. A. Pulgarín-Agudelo, O. Vigil-Galán, A. Pérez-Rodríguez and E. Saucedo, *J. Am. Chem. Soc.*, 2012, **134**, 8018–8021.
22 S. López-Marino, Y. Sánchez, M. Placidi, A. Fairbrother, M. Espindola-Rodríguez, X. Fontané, V. Izquierdo-Roca, J. López-García, L. Calvo-Barrio, A. Pérez-Rodríguez and E. Saucedo, *Chem. – Eur. J.*, 2013, **19**, 14814–14822.
23 L. Guen and W. S. Glaunsinger, *J. Solid State Chem.*, 1980, **35**, 10–21.
24. NIST: X-Ray Mass Attenuation Coefficients - Table 3, http://physics.nist.gov/PhysRefData/XrayMassCoef/tab3.html, last time accessed 2016-02-16.
25 J. Rodríguez-Carvajal, *Phys. B Condens. Matter*, 1993, **192**, 55–69.
26 P. Thompson, D. E. Cox and J. B. Hastings, *J. Appl. Crystallogr.*, 1987, **20**, 79–83.
27 H. M. Rietveld, *J. Appl. Crystallogr.*, 1969, **2**, 65–71.
28 A. Le Bail, H. Duroy and J. L. Fourquet, *Mater. Res. Bull.*, 1988, **23**, 447–452.
29 L. W. Finger, D. E. Cox and A. P. Jephcoat, *J. Appl. Crystallogr.*, 1994, **27**, 892–900.
30 G. Caglioti, A. Paoletti and F. P. Ricci, *Nucl. Instrum.*, 1958, **3**, 223–228.
31 J. Rodríguez-Carvaja, lStudy of Micro-Structural effects by powder diffraction using the Program FULLPROF. Laboratoire Léon Brillouin (CEA-CNRS), CEA/Saclay, 91191 Gif sur Yvette Cedex. 2003.
32 P. M. P. Salomé, J. Malaquias, P. A. Fernandes, M. S. Ferreira, A. F. da Cunha, J. P. Leitão, J. C. González and F. M. Matinaga, *Sol. Energy Mater. Sol. Cells*, 2012, **101**, 147 – 153.
33 S. Siebentritt and S. Schorr, *Prog. Photovolt. Res. Appl.*, 2012, **20**, 512–519.
34 A. Fairbrother, X. Fontané, V. Izquierdo-Roca, M. Placidi, D. Sylla, M. Espindola-Rodriguez, S. López-Mariño, F. A. Pulgarín, O. Vigil-Galán, A. Pérez-Rodríguez and E. Saucedo, *Prog. Photovolt. Res. Appl.*, 2014, **22**, 479–487.
35 A. Walsh, S. Chen, S.-H. Wei and X.-G. Gong, *Adv. Energy Mater.*, 2012, **2**, 400–409.
36 M. Dimitrievska, A. Fairbrother, E. Saucedo, A. Pérez-Rodríguez and V. Izquierdo-Roca, *Sol. Energy Mater. Sol. Cells*, 2016, **149**, 304–309.
37 M. Dimitrievska, A. Fairbrother, X. Fontané, T. Jawhari, V. Izquierdo-Roca, E. Saucedo and A. Pérez-Rodríguez, *Appl. Phys. Lett.*, 2014, **104**, 021901.
38 D. Nam, S. Cho, J.-H. Sim, K.-J. Yang, D.-H. Son, D.-H. Kim, J.-K. Kang, M.-S. Kwon, C.-W. Jeon and H. Cheong, *Sol. Energy Mater. Sol. Cells*, 2016, **149**, 226–231.
39 X. Liu, Y. Feng, H. Cui, F. Liu, X. Hao, G. Conibeer, D. B. Mitzi and M. Green, *Prog. Photovolt. Res. Appl.*, 2016, n/a–n/a.
40 M. Dimitrievska, H. Xie, A. J. Jackson, X. Fontané, M. Espíndola-Rodríguez, E. Saucedo, A. Pérez-Rodríguez, A. Walsh and V. Izquierdo-Roca, *Phys. Chem. Chem. Phys.*, 2015 (doi: 10.1039/C5CP04498G).
41 M. Dimitrievska, G. Gurieva, H. Xie, A. Carrete, A. Cabot, E. Saucedo, A. Pérez-Rodríguez, S. Schorr and V. Izquierdo-Roca, *J. Alloys Compd.*, 2015, **628**, 464–470.
42 G. K. Williamson and W. H. Hall, *Acta Metall.*, 1953, **1**, 22–31.
43 J. J. Scragg, P. J. Dale, D. Colombara and L. M. Peter, *ChemPhysChem*, 2012, **13**, 3035–3046.
44 H. Xin, J. K. Katahara, I. L. Braly and H. W. Hillhouse, *Adv. Energy Mater.*, 2014, **4**, 11.
45 M. Werner, D. Keller, S. G. Haass, C. Gretener, B. Bissig, P. Fuchs, F. La Mattina, R. Erni, Y. E. Romanyuk and A. N. Tiwari, *ACS Appl. Mater. Interfaces*, 2015, **7**, 12141–12146.
46 T. Schnabel, T. Abzieher, T. M. Friedlmeier and E. Ahlswede, *Photovolt. IEEE J. Of*, 2015, **5**, 670–675.